Accelerated discovery of crystalline materials with record ultralow lattice thermal conductivity via a universal descriptor

Xingchen Shen, Jiongzhi Zheng, Michael Marek Koza, Petr Levinsky, Jiri Hejtmanek, Philippe Boullay, Bernard Raveau, Jinghui Wang, Jun Li, Pierric Lemoine, et al.

nature communications

Article

https://doi.org/10.1038/s41467-025-67333-z

Accelerated discovery of crystalline materials with record ultralow lattice thermal conductivity via a universal descriptor

Received: 17 July 2025

Accepted: 27 November 2025

Published online: 17 December 2025

Check for updates

Xingchen Shen[1,2,8] ✉, Jiongzhi Zheng[3,8], Michael Marek Koza[4], Petr Levinsky[5], Jiri Hejtmanek[5], Philippe Boullay[2], Bernard Raveau[2], Jinghui Wang[6], Jun Li[6], Pierric Lemoine[7], Christophe Candolfi[7] & Emmanuel Guilmeau[2] ✉

Ultralow glass-like lattice thermal conductivity in crystalline materials is crucial for enhancing energy conversion efficiency in thermoelectrics and thermal insulators. We introduce a universal descriptor for thermal conductivity that relies only on the atomic number in the primitive cell and the sound velocity, enabling fast and scalable materials screening. Coupled with high-throughput workflows and universal machine learning potentials, we identify the candidate materials with ultralow thermal conductivity from over 25, 000 materials. We further validate this approach by experimentally confirming record-low thermal conductivity values of 0.15–0.16 W/m·K from 170 to 400 K in the halide metal $CsAg_2I_3$. Combining inelastic neutron scattering with first-principles calculations, we attribute the ultralow thermal conductivity to the intrinsically small sound velocity, strong anharmonicity, and structural complexity. Our work illustrates how a universal descriptor, combined with high-throughput screening, machine-learning potential and experiment, enables the efficient discovery of materials with ultralow thermal conductivity.

The discovery of crystalline materials with ultralow glass-like lattice thermal conductivity (ULG-type κ_L) is essential for maximizing performance in thermoelectrics[1], thermal insulators[2], and thermal coating barriers[3]. Generally, crystalline materials with complex structures, large primitive cells (containing a number of atoms >20), and heavy elements tend to exhibit low κ_L[4]. However, ultralow κ_L[5] can also occur in materials with small primitive cells and light elements, which is due to the presence of rattler atoms[6], strong lattice anharmonicity[7,8], or bonding heterogeneity[9]. Recently, significant progress has been made in both experimental and theoretical investigations aimed at uncovering crystalline materials with very low κ_L below 1.0 W/m·K. Experimentally, Mukhopadhyay et al.[10] developed a class of thallium selenides and measured an ultralow κ_L of approximately 0.30 W/m·K at 300 K in Tl_3VSe_4. This value was attributed to its exceptionally low group velocity and strong anharmonicity. Acharyya et al.[11] synthesized a layered halide perovskite $Cs_3Bi_2I_6Cl_3$ single crystal and measured an

[1]MOE Key Laboratory of Materials Physics and Chemistry under Extraordinary Conditions, School of Physical Science and Technology, Northwestern Polytechnical University, Xi'an, China. [2]CRISMAT, CNRS, Normandie Univ, ENSICAEN, UNICAEN, Caen, France. [3]Thayer School of Engineering, Dartmouth College, Hanover, NH, USA. [4]Institute Laue Langevin, 71 avenue des Martyrs CS 20156, Grenoble, Cedex 9, France. [5]FZU - Institute of Physics of the Czech Academy of Sciences, Cukrovarnická 10/112, Prague, Czech Republic. [6]ShanghaiTech Laboratory for Topological Physics & School of Physical Science and Technology, ShanghaiTech University, Shanghai, China. [7]Université de Lorraine, CNRS, IJL, Nancy, France. [8]These authors contributed equally: Xingchen Shen, Jiongzhi Zheng. ✉e-mail: xingchen.shen@nwpu.edu.cn; emmanuel.guilmeau@ensicaen.fr

ultralow thermal conductivity of 0.20 W/m·K along in-/cross-plane directions at 300 K, which was attributed to its low average sound velocity (υ) and weak chemical bonds. Gibson et al.[12] found that the 2D layered structure of mixed anion $Bi_4O_4SeCl_2$ with a specific spatial arrangement of interfaces suppresses acoustic phonon contributions, achieving an ultralow κ_L of 0.10 W/m·K in the cross-plane direction at 300 K. Interestingly, for the even more complex crystal structure of argyrodite Cu_7PS_6 with 54 atoms in primitive cell, Shen et al.[13] reported an ultralow κ_L of 0.50 W/m·K at 300 K. Notably, these crystalline materials with ultralow κ_L also generally exhibit a weak/positive temperature-dependent behavior, resembling ULG-type thermal conduction. These experimental observations of ULG-type κ_L raise an open question: how can κ_L be pushed to its lower limit over a broad temperature range based on material properties, such as anharmonicity and structural complexity?

Theoretically, to accurately explain the experimental ULG-type κ_L, Simoncelli et al.[14] proposed a unified theory of thermal transport that considers both particle-like phonon propagation (phonon contribution) and wave-like tunneling channels (diffuson contribution), successfully reproducing the glass-like temperature dependence of κ_L in crystalline $CsPbBr_3$. Building on the unified theory of thermal transport, Xia et al.[15] further incorporated the effects of anharmonic temperature dependence and higher-order phonon scattering, successfully replicating the temperature-independent ultralow κ_L in crystalline $Cu_{12}Sb_4S_{13}$. Moreover, the well-established unified theory of thermal transport has been successfully applied to explain thermal transport in various materials with complex structures or strong anharmonicity, such as $Yb_{11}M_4Sb_{11}$ (M=Mg and Mn)[16], Cu_7PS_6[13], $NaAg_3S_2$[17], $K_2Ag_4Se_3$[18], $YbFe_4Sb_{12}$[19], and $MAPbI_3$ (MA=methylammonium)[20]. Therefore, exploring materials with ULG-type κ_L, approaching the glassy limit in crystalline compounds, is not only fundamentally intriguing but also essential for understanding the complex interplay between crystal structure, bonding strength, and anharmonic lattice dynamics. These investigations offer valuable criteria for identifying unknown low-κ_L crystalline materials and open new avenues for engineering heat transport properties in existing compounds.

Despite significant advancements in experimental observations and theoretical predictions of κ_L in crystalline materials, the high cost remains a major obstacle to high-throughput calculations and experiments, as well as the rapid screening of crystalline materials with ULG-type κ_L. To simplify the theoretical prediction process for identifying materials with ultralow κ_L, Knoop et al.[21] introduced the concept of the degree of anharmonicity (DOA), derived from ab initio molecular dynamics (AIMD), to quantitatively evaluate κ_L in crystalline materials. Using the concept of DOA, Zeng et al.[22] theoretically and experimentally reported an ultralow κ_L of 0.25 W/m·K at 300 K in the simple crystalline material $AgTlI_2$, attributed to its Ag-associated strong anharmonicity. Additionally, considering the inverse relationship between population/diffuson thermal conductivity and number of atoms in a primitive cell (n), they proposed a conceptual diagram to facilitate the search for ultralow κ_L crystalline materials with a simple crystal structure. Although the AIMD-based DOA concept facilitates the rapid screening of materials with ultralow κ_L, the lengthy AIMD calculations remain computationally expensive, and the DOA concept is limited to qualitatively evaluating thermal transport properties.

Over the past decades, widely known empirical thermal transport models, such as the Slack[23] and Debye-Callaway[24] models, have been proposed to estimate the thermal conductivity of crystalline materials. However, these models are limited in accuracy and rely heavily on numerous empirical parameters. To overcome the limitations of the aforementioned empirical models, several have proposed an improved and straightforward minimum thermal conductivity model based on diffuson-mediated thermal transport theory. Furthermore, inspired by the unified theory of thermal transport, Xia et al.[25] recently proposed a minimum thermal conductivity model that incorporates contributions from both propagons and diffusons. Meanwhile, Wang et al.[26] derived an interpretable formula for κ_L of crystals by utilizing a large database and building upon the Slack model. Although recently developed thermal transport models have achieved significant success, their complexity[25,26] or limited prediction accuracy[27] hinders their practical application by experimentalists. A simple unified thermal transport indicator based on experimentally accessible parameters has still not yet been developed, posing a significant challenge to the efficient exploration of crystalline materials with desirable thermal transport properties. In addition, with the rapid advancements in universal machine learning force fields (MLFF), such as MACE[28], M3GNET[29], CHGNET[30], and MatterSim[31], integrating MLFF into a universal thermal transport indicator has become essential.

In this work, we introduce a universal macroscopic descriptor (σ) that enables effective screening of ULG-type κ_L in crystalline materials. This descriptor is expressed in a simple form involving only the sound velocity (υ) and the atomic number of the primitive cell (n). Using a large and diverse set of experimental and theoretical data, we established this universal descriptor by identifying a highly correlated Pearson-type relationship and systematically simplifying the Slack model based on fundamental physical quantities. We further integrated this universal descriptor with high-throughput workflows and universal machine-learning interatomic potentials to screen for materials with ultralow κ_L across the Materials Project database[32]. We identified two metal halides in the CsA_2I_3 (A = Ag, Cu) system as promising ULG-type candidates. We subsequently synthesized $CsAg_2I_3$ and $CsCu_2I_3$ and experimentally confirmed ULG-type κ_L values of 0.15–0.16 W/m·K between 170 and 400 K and 0.18–0.20 W/m·K between 300 and 523 K, respectively. Moreover, using a combination of state-of-the-art techniques, including electron diffraction, inelastic neutron scattering, and a unified theory of thermal transport, we comprehensively investigated the relationships among crystal structure, lattice dynamics, and microscopic thermal transport in the representative compound $CsAg_2I_3$. Our work introduces an effective and accessible tool, readily usable by both experimentalists and theoreticians, for screening crystalline materials with targeted ULG-type κ_L. By establishing a robust correlation between ULG-type thermal transport and laboratory-measurable physical quantities, this study significantly accelerates the discovery of materials for a broad range of thermal-related applications.

Results and discussion

Potential indicator for screening ULG-type κ_L materials

Using the oversimplified elementary kinetic transport theory, κ_L can be computed as $\kappa_L = \frac{1}{3} C_V \upsilon_g l$, where C_v is the isochoric heat capacity, υ_g is the phonon group velocity, and l is the phonon mean free path. Therefore, a high υ_g inherently results in a high lattice thermal conductivity[33]. For instance, Li et al.[33] demonstrated a well-linearized relationship between the minimum thermal conductivity and the υ_g for various crystalline materials. Additionally, for crystalline materials with ultralow κ_L, Agne et al.[27] derived a minimum diffuson-mediated thermal transport model: $\kappa_{L,\,min} = 0.76(n_d)^{2/3} k_B * \frac{1}{3}(2\upsilon_t + \upsilon_l)$, where n_d is the atomic number density, k_B is the Boltzmann constant, and υ_t and υ_l are the transverse and longitudinal sound velocities, respectively. Recently, Wang et al.[26] also derived an interpretable formula for the κ_L of crystals: $\kappa_L = \frac{G\upsilon V^{1/3}}{\gamma T^{\delta}} * e^{-r}$, where G, V, r, and δ are shear modulus, volume of the primitive cell, Grüneisen parameters, and scattering parameter (between 1 and 2). This formula achieves high precision and provides fast predictions. Within the framework of Slack model and some predictive models of minimum κ_L[23,25–27], various empirical macroscopic quantities are considered as potential correlated parameters influencing ULG-type κ_L, such as Debye temperature (Θ_D), n, volume per atom (V_a), density (ρ), average mass of atoms (M_a), and isobaric

https://doi.org/10.1038/s41467-025-67333-z

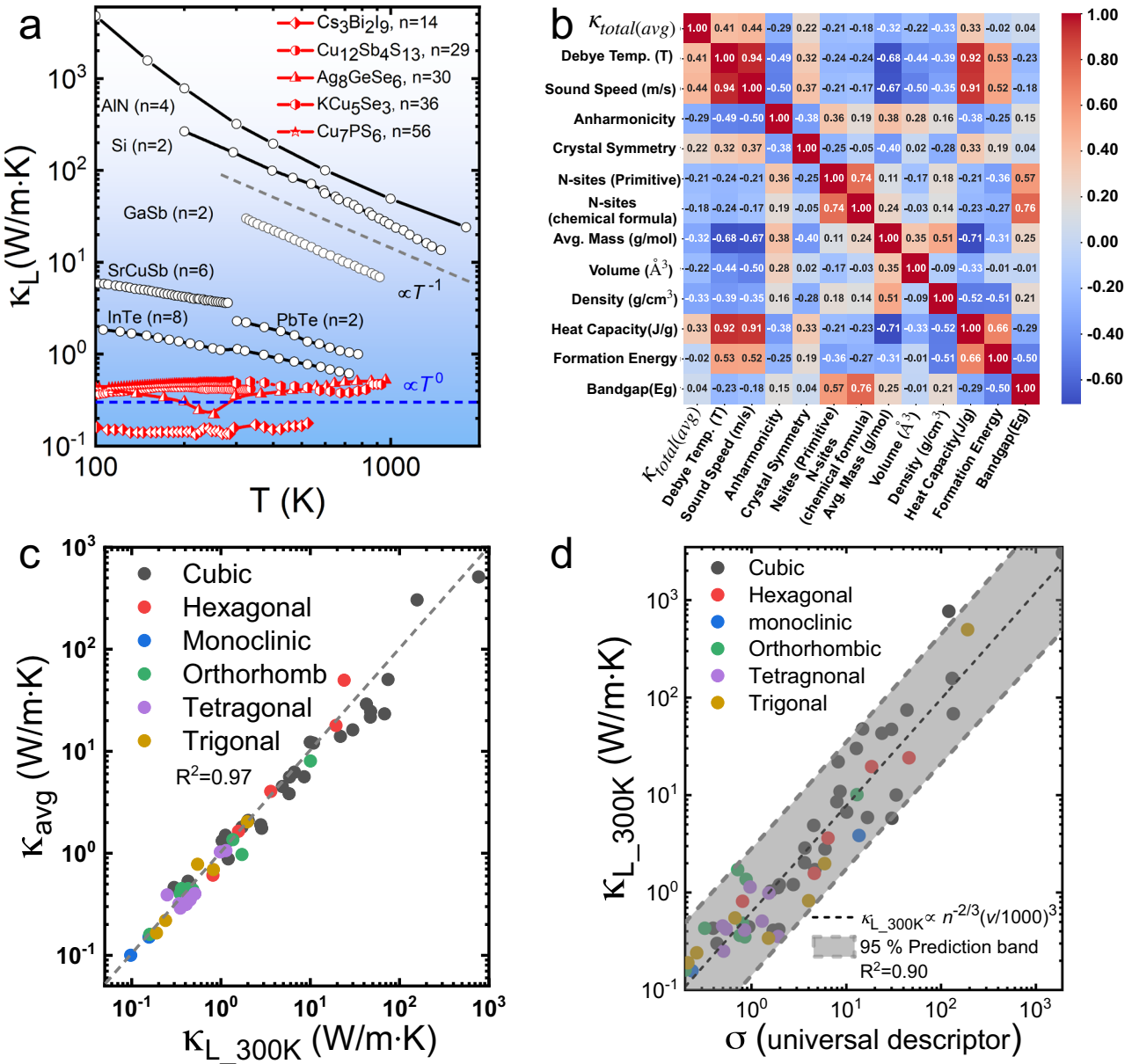

Fig. 1 | Construction of a universal descriptor for screening ULG-type κ_L. **a** Experimental κ_L for various compounds, including Si, AlN, GaSb, PbTe, InTe, SrCuSb, $Cs_3Bi_2I_9$, $Cu_{12}Sb_4S_{13}$, Ag_8GeSe_6, KCu_5Se_3, and Cu_7PS_6. **b** The Pearson correlation matrix calculations of over 40 crystalline materials. Note that the crystal anharmonicity was evaluated using the method proposed by Knoop et al.[21]. **c** The plot of the experimental κ_{avg} vs. κ_{L_300K} of over 60 crystalline samples. **d** The plot of the experimental κ_{L_300K} vs. σ of over 60 crystalline samples. Detailed information on the experimental and calculated data shown in Fig. 1b–d are listed in Table S1a, b in the Supplementary Information (SI).

heat capacity (C_p). To evaluate the correlation between these microscopic quantities, we conducted a Pearson correlation matrix analysis.

To propose a model for assessing ULG-type κ_L in crystalline materials, we analyze the relationship between temperature-dependent κ_L and n. As illustrated in Fig. 1a, the κ_L of crystalline materials typically exhibits a universal asymptotic decay, expressed as $\kappa_L(T) \sim T^{-m}$ [34]. Specifically, the dominant anharmonic three-phonon scattering mechanisms leads to a trend of $\kappa_L(T) \propto T^{-1}$ ($m = 1$)[35], as observed in strongly-bonded materials, such as AlN[36], Si[37], and GaSb[38]. Strong anharmonic phonon scattering events result in milder decays ($m < 1$), as seen in $\kappa_L(T)$ behavior of PbTe ($T^{-0.92}$)[39], InTe ($T^{-0.55}$)[40,41], and SrCuSb ($T^{-0.51}$) compounds[42]. In contrast, in highly disordered or glassy materials, $\kappa_L(T)$ exhibits a temperature independence or even positive temperature dependence, as seen in $Cs_3Bi_2I_9$[43], $Cu_{12}Sb_4S_{13}$[44], Ag_8GeSe_6[45], KCu_5Se_3[46], and Cu_7PS_6[13]. Macroscopically, compounds with a higher number of n generally show a greater tendency to display weak or positive temperature dependence in κ_L, which can be considered a critical factor in capturing the glass-like behavior of thermal conductivity.

To qualitatively assess the magnitude of ULG-type κ_L in crystalline materials, we utilized experimental κ_{avg}, obtained as the average of the κ_L over measured temperatures (Table S1a). We considered the κ_L values above the Debye temperature for specific crystalline materials, as this temperature range is dominated by phonon-phonon Umklapp scattering. Our Pearson correlation matrix analysis (Fig. 1b) shows that v has the strongest positive correlation value with κ_{avg} (0.44), suggesting that ultralow v can serve as a practical and direct parameter for identifying ULG-type κ_L. Collectively, Θ_D, v, anharmonicity, crystal symmetry (designated by the space group number), n, M_a, V_a, C_p, number of atoms in the chemical formula, and ρ account for about 98%

of the correlation with κ_{avg}. In contrast, parameters like formation energy and band gap present negligible correlation (2%).

To simplify the prediction of ULG-type κ_L using physical quantities, we begin with a classical Slack model of κ_L[47,48], under dominant Umklapp scattering:

$$\kappa_L \approx A\frac{M_a\Theta_D{}^3V_a{}^{1/3}}{\gamma^2 n^{2/3}T} \quad (1)$$

where A is a constant. Given that γ is not constant but typically varies between 1 and 2 in most crystalline materials, we employ a proportional relationship:

$$\kappa_L \propto \frac{M_a\Theta_D{}^3V_a{}^{1/3}}{n^{2/3}T} \quad (2)$$

Considering that optical phonons can contribute significantly to thermal conductivity[49,50] and to develop a universal lattice thermal-conductivity descriptor applicable to both diffuson- and phonon-dominated regimes, we adopt the traditional definition of the Debye temperature, rather than the acoustic-mode Debye temperature. The traditional Debye temperature Θ_D can be expressed by the relation[51] $\Theta_D = \frac{\hbar v}{k_B}\left(\frac{3}{4\pi}\frac{n}{V}\right)^{1/3} = \frac{\hbar v}{k_B}\left(\frac{3}{4\pi}\frac{1}{V_a}\right)^{1/3}$, which we rewrite in the following form:

$$\kappa_L \propto \frac{3\hbar^3}{4\pi k_B{}^3}\frac{M_a v^3}{V_a{}^{2/3}n^{2/3}T} \propto \frac{M_a v^3}{V_a{}^{2/3}n^{2/3}T} \quad (3)$$

Figure 1c plots the relationship between κ_{L_300K} and κ_{ave} (Table S1b), which reveals a strong linear positive correlation. This indicates that crystalline materials with low κ_{L_300K} also tend to have a low κ_{ave}. Therefore, κ_{ave} can be approximated by the following expression:

$$\kappa_{ave} \propto \kappa_{L\_300K} \propto \frac{M_a}{V_a{}^{2/3}}\frac{v^3}{n^{2/3}} \quad (4)$$

After several trials of the possible indicators in formula (4), including $M_a{}^*(v/1000)^3$, $M_a{}^*n^{-\frac{2}{3}}$, $n^{-\frac{2}{3}}(v/1000)^3$, $M_a{}^*(v/1000)^3{}^*n^{-\frac{2}{3}}$, and $M_a{}^*(v/1000)^3{}^*(n^*V_a)^{-\frac{2}{3}}$, we identified an indicator σ, expressed as $n^{-\frac{2}{3}}(v/1000)^3$, that exhibits a linear relation with κ_{avg}, achieving a goodness of fit of 0.9. Other fitting results between κ_{L_300K} and indicators ($M_a{}^*(v/1000)^3$, $M_a{}^*n^{-\frac{2}{3}}$, $M_a{}^*(v/1000)^3{}^*n^{-2/3}$, and $M_a{}^*(v/1000)^3{}^*(n*V_a)^{-\frac{2}{3}}$) can be found in Fig. S1. As shown in Fig. 1d, we collected experimental κ_{L_300K}, including both ultrahigh and ultralow values, as well as v and n values from over 60 crystalline materials with various crystal structures (Table S1b). κ_{L_300K} typically follows a linear relationship with the established σ on a log scale. Our modeling indicates that almost all data points fall within the gray region, representing a 95% confidence and prediction band. This behavior strongly supports the correctness of the proposed indicator σ, suggesting its effectiveness in identifying ULG-type κ_L crystalline materials without the need for time-consuming calculations of κ_L. However, experimental determination and validation of v still require material synthesis and characterization, which can be time- and energy-intensive for cross-checking.

To overcome this limitation, we conducted high-throughput calculations using a universal machine learning force field method (MACE[28]) to enhance the efficiency and accuracy of v estimations. As illustrated in Fig. 2, we utilized the Materials Project database[32] containing 153,902 materials and applied various screening criteria. These included selecting only non-magnetic compounds, limiting the number of different element types to less than four, restricting the number of atomic sites to less than 60, requiring a band gap greater than 0 eV, and ensuring the energy above the hull was below 0.1 eV/atom.

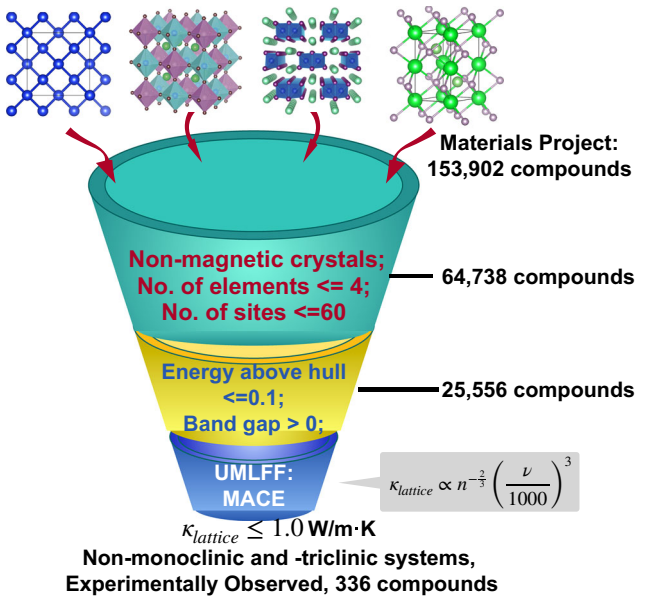

Fig. 2 | Schematic diagram of high-throughput screening process. High-throughput thermal conductivity calculations using MACE[28] and our universal indicator. The crystal structures were visualized and exported using the VESTA software package[92].

Applying these criteria, we filtered the dataset down to 25,556 materials. We then integrated the universal machine learning force field package MACE[28] with our indicator to predict thermal conductivity. After obtaining the predicted values, we further excluded the low-symmetry systems, i.e., monoclinic and triclinic lattices and considered only crystals identified as experimentally observed in the Materials Project[47]. As a result, we identified only 336 materials with a thermal conductivity below 1.0 W/m·K. Given that metal halides consistently exhibit low thermal conductivity[11,43,50,52,53], we selected their analogs, specifically crystalline $CsAg_2I_3$ and $CsCu_2I_3$, from 336 compounds for further experimental investigation.

Structural evolution and thermal transport properties

In combination of high-throughput calculations with machine learning techniques (see the method section), we screened metal halides CsA_2I_3 (A = Ag, Cu) and synthesized them for characterizations of their structural and physical properties. Prior studies reported that $CsAg_2I_3$ adopts an orthorhombic crystal structure of *Pnma* space group (No 62)[54,55], while the structural analog $CsCu_2I_3$ crystallizes in the higher-symmetry *Cmcm* space group (No 63), as plotted in Fig. S2. The corresponding Rietveld refinements of powder X-ray diffraction (PXRD) patterns of the $CsAg_2I_3$ and $CsCu_2I_3$ samples at 300 K confirm their high-purity (Figs. S3–S4). The refined crystallographic data for the two compounds are provided in Table S2–S3. The microscopic morphology and chemical distributions of all the samples, examined using SEM and SEM-EDX, are presented in Figs. S5–S6.

To analyze the phase stability of $CsAg_2I_3$, PXRD patterns were recorded from 250 to 320 K at Cu wavelength with 10 K intervals (Fig. S7). Enlargement of the PXRD patterns reveals that, as the temperature increases, certain diffraction peaks gradually disappear, as exemplified by the peaks observed at 2θ = 22.46°, 27.20°, and 28.07° at T = 250 K. In addition, some peaks shift significantly to lower angles, such as those observed at 2θ = 28.83°, 30.68°, and 31.71° at T = 250 K and at 2θ = 28.55°, 30.41°, and 31.43°, respectively, at T = 320 K. Such peak intensity and position modifications suggest the existence of a structural modification of $CsAg_2I_3$ around room temperature. Analyses (Fig. S8, see details in the SI) support the assumption that crystal structure of $CsAg_2I_3$ evolves gradually from 250 to 320 K from its

distorted variant crystal structure reported in *Pnma* space group (Fig. S9a, b) to that reported for $CsCu_2I_3$[56], a crystal structure of higher symmetry in *Bbmm/Cmcm* space group (Fig. S9c, d). Besides, a pronounced minor peak was observed at 278 K in the C_p data (Fig. S10), which probably corresponds to a subtle symmetry modification in $CsAg_2I_3$, supporting the results of the PXRD data. The second peak over a broad temperature range of 285-310 K originates from the typical transition of addenda for the low-temperature C_p measurement.

The measured κ_L of all sintered polycrystalline samples is displayed in Fig. 3a. The $CsAg_2I_3$ sample exhibits a temperature-independent κ_L of 0.15–0.16 W/m·K from 170 to 400 K, whereas the $CsCu_2I_3$ sample shows values of 0.18–0.20 W/m·K from 300 to 523 K. Notably, compared to other metal halides[11,52,57–59], the CsA_2I_3 (A = Ag, Cu) samples exhibit the lowest κ_L values across a broad temperature range, validating the practical effectiveness of combining a universal descriptor with high-throughput workflows and universal machine-learning interatomic potentials. Our primary experimental objective is to demonstrate the successful identification of crystalline materials with the ULG-type κ_L; detailed microscopic analysis of the slight differences in κ_L between $CsAg_2I_3$ and $CsCu_2I_3$ falls outside the scope of this study. To correlate thermal transport properties to crystal structures, we conducted structural and chemical bonding analyses. Since these two samples share structural similarity in the high-temperature *Bbmm/Cmcm* phase, we selected a representative compound, $CsAg_2I_3$, for further detailed discussions. The *Bbmm* structure of the 320 K-form of $CsAg_2I_3$ (Fig. 3b) consists of $[Ag_2I_3]^-$ double chains of edge-sharing AgI_4 tetrahedra running along *b* (Fig. 3b), interconnected by (100) layers of Cs^+ cations. Remarkably, the Ag-I distances, ranging from 2.78 to 2.92 Å, are significantly smaller than that expected from the sum of ionic radii (r_{Ag+}= 1 Å, r_{I-}=2.2 Å). The stability of the structure is clearly ensured by the ionic character of the Cs-I bonds between the $[Ag_2I_3]^-$ double chains. Each Cs^+ cation exhibits eight nearest I^- neighbors with Cs-I distances ranging from 3.93 to 4.18 Å, close to the sum of ionic radii (r_{Cs+}=1.7 Å, r_{I-}=2.2 Å), forming almost regular CsI_8 bicapped trigonal prisms sharing faces along *b* and edges along *c*.

The *Pnma* structures of the low temperature form of $CsAg_2I_3$ (i.e. 100 K and 250 K, Fig. 3c-d) is very similar to the *Bbmm* form (Fig. 3b). The $[Ag_2I_3]^-$ double chains of edge-sharing AgI_4 tetrahedrons (Fig. 3c) are only slightly distorted with Ag-I distances, ranging from 2.78 to 2.97 Å (Fig. 3e-f). Previously aligned along the *c*-axis in the *Bbmm* form (Fig. 3b), the $[Ag_2I_3]^-$ double chains are now tilted around the *b*-axis and in antiphase along *a* (Fig. 3c). This tilting is slightly more pronounced at 100 K than at 250 K (Fig. 3c, d), in line with the simultaneous increase in the *c* lattice parameter and the decrease in the *a* lattice parameter as the temperature decreases (Fig. S8). It is accompanied by a displacement of Cs^+ cations within the (001) plane (Fig. 3c), leading to a significant change in the geometry of the $[CsI_3]$ layers (Fig. 3b). Each Cs^+ cation now exhibits seven nearest I^- neighbors with Cs-I distances ranging from 3.86 to 4.07 Å (Fig. 3e, f), forming quasi-regular CsI_7 monocapped trigonal prisms. Two additional I neighbors corresponding to larger Cs-I distances (4.28 to 4.45 Å) are observed which may not be considered as pure ionic bonds. As a consequence, the structure can be described as (100) $[CsI_3]$ layers built up of CsI_7 monocapped trigonal prisms sharing faces along *b* and apices along *c* (Fig. 3c).

Such a soft topotactic transition from the high temperature to the low temperature form is explained by the fact that the I(1a) and I(1b) anions in the low temperature *Pnma* form at the border of the $[Ag_2I_3]^-$ double chains are only linked to two Ag^+ cations and consequently can move easily contrary to the I(2) anions located inside the chains which are blocked by 4 Ag^+ cations. This is supported by the atomic displacement parameters (ADPs) obtained from both PXRD (Table S4) and 3D ED (Table S8), which show that the I(1a) and I(1b) atoms have higher ADPs than the I(2) atom (Fig. 3e, f). With 3D ED, anisotropic ADPs could be refined, revealing that while I(2) atoms display nearly isotropic ADPs with only slight anisotropy, I(1a) and I(1b) exhibit pronounced anisotropy (Fig. 3f) along a direction associated with the rotation of the $[Ag_2I_3]^-$ double chains.

This structural analysis emphasizes the key role of iodine vibration in the thermal conductivity of the low temperature form of $CsAg_2I_3$ compound. It suggests that I^- governs the appearance of ultralow thermal conductivity in connection with the one-dimensional character of the structure. The 1D character of the double $[Ag_2I_3]^-$ anionic chains facilitates the phonon propagation along the *b* axis, so that higher κ_L^P can be expected along this direction. These anisotropic transport properties are moreover reinforced by the fact that the central "Ag-I(2)-Ag" chains form very strong bonds as the I(2) atom is blocked between four Ag^+ cations. In contrast, the I(1a) and I(1b) atoms located at the junction between the CsI_7 monocapped prisms and the $[Ag_2I_3]^-$ chains are freer due to the fact that they are linked to only two Ag^+ cations. Consequently, larger ADPs likely contribute to pronounced anharmonicity at these atomic positions. Such a feature is favorable to the suppression of phonon propagation, leading to lower κ_L^P values in the directions transversal to the *b*-axis. In the high temperature *Bbmm* form the distribution of the I^- anions is more symmetric, leading to more regular AgI_4 tetrahedrons and a more symmetric distribution of the I(1) anionic species (instead of I(1a) and I(1b)). These features are expected to facilitate the phonon transport, increasing κ_L^P along the *a*- and *c*-axis. As shown in Table S9a, the experimental average sound velocity ($\nu_{a,\,exp}$) of 1188 m/s is considerably lower than that of most thermoelectric materials[28]. The measured $\nu_{a,\,exp}$ aligns well with the calculated value of 1125 m/s, as listed in Table S9b, indicating the weak bonding and soft atomic lattices of $CsAg_2I_3$ compound, which might contribute to the low $\nu_{a,\,exp}$, reduced elastic properties, significant anharmonicity, and ultimately ultralow κ_L.

Lattice dynamics and strong anharmonicity

For better understanding the ultralow κ_L of $CsAg_2I_3$, we conducted temperature-dependent inelastic neutron scattering (INS) to study the lattice dynamics properties. Details on the INS technique and data processing are provided in the SI. Measurements were performed with two incident energies, E_i = 12.5 and 30.0 meV, across a wide temperature range of 1.5-300 K, enabling us to analyze the complete generalized density of states (GDOS) as well as the temperature evolution of low-energy phonons. As illustrated in Fig. S11, contour maps of neutron scattering intensity, the dynamic structure factor $S(|\mathbf{Q}|, E)$ measured with a higher incident energy E_i = 30.0 meV, reveals prominent low-energy phonon modes below 5 meV at 1.5 K. Furthermore, we processed the calculated phonon density of states (PDOS) at 0 K by convoluting it with the experimental resolution and applying elemental neutron weighted cross-sections. Note that the calculated neutron weighted PDOS is in close agreement with the experimental GDOS obtained with E_i = 30.0 meV at 1.5 K (see Fig. 4d).

Figure 4a depicts $S(|\mathbf{Q}|, E)$ measured with E_i = 12.5 meV at 1.5 K. The measured signal discloses two low-energy phonon bands of high intensity located at about 2 and 3.3 meV and two less intense modes centered around 5 and 7 meV. They are visible as clearly separated peaks in the corresponding GDOS presented in Fig. 4d. The computed element-projected PDOS shown with the experimental data suggests that these low-energy flat bands are dominated by Ag- and I-weighed phonon modes. Interestingly, as indicated by the computed phonon dispersion (blue lines denote acoustic phonon branches; white lines denote optical phonon branches) in Fig. 4a, b strongly dispersive feature can be observed around $|\mathbf{Q}|$ = 2.5–3.0 $Å^{-1}$. It is characteristic of acoustic phonons. These acoustic phonons exhibit thus an exceptionally low cut-off frequency by crossing the low-energy optical phonons at 1 ~ 2 meV. We expect this phonon dispersion to be a favorable configuration for efficient phonon-phonon scattering.

https://doi.org/10.1038/s41467-025-67333-z

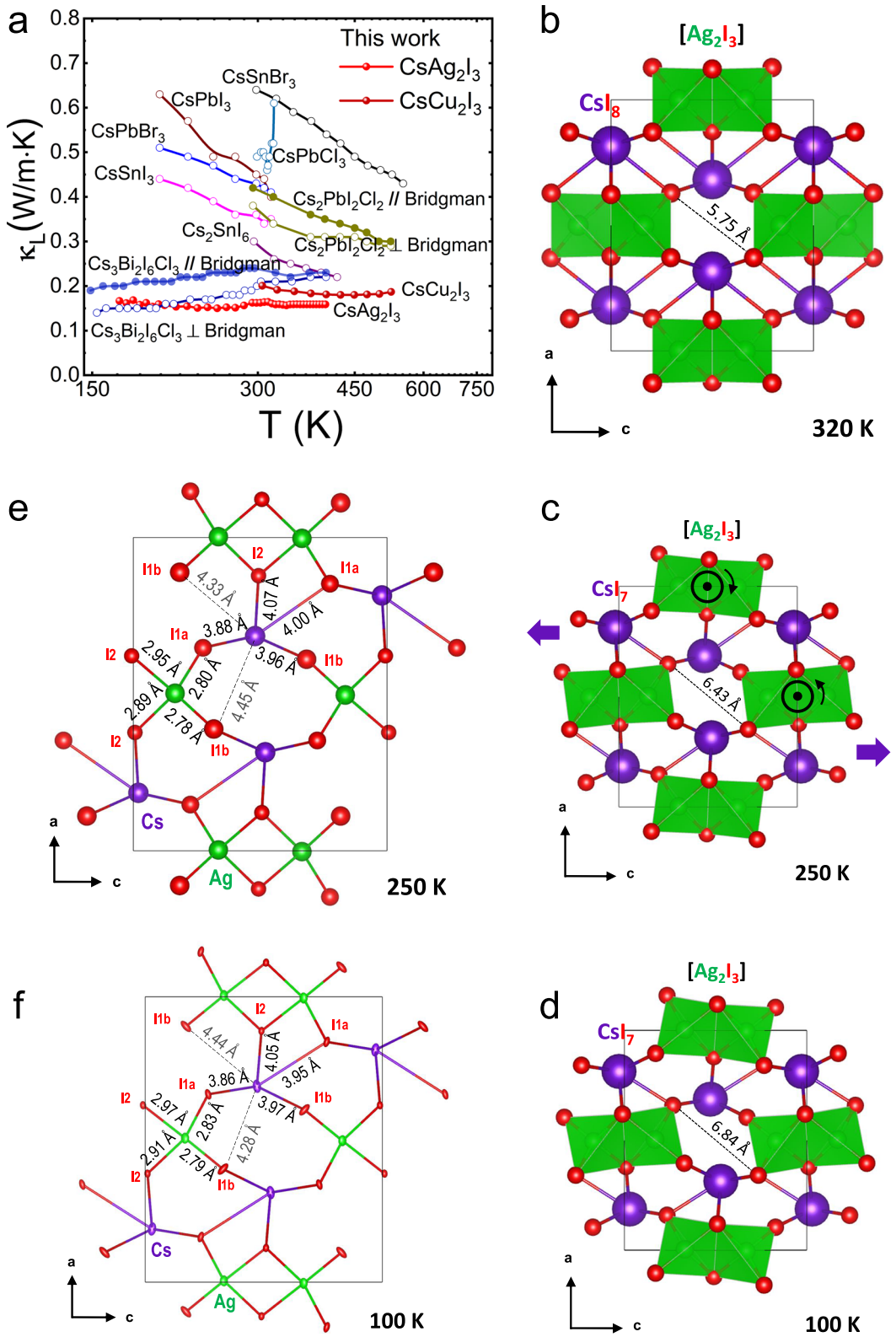

Fig. 3 | Thermal conductivities and structural characterizations of CsA_2I_3 (A = Ag, Cu) compounds. a Comparison κ_L of $CsAg_2I_3$ and $CsCu_2I_3$ with other metal halides compounds[11,52,57–59]. Evolution of the crystal structures of $CsAg_2I_3$ with temperature, as determined by **b** PXRD at 320 K, **c** PXRD at 250 K, and **d** 3D ED at 100 K. Crystal structure of $CsAg_2I_3$ (SG: *Pnma*) projected along [010], as obtained from **e** PXRD data recorded at 250 K and **f**, single-crystal 3D ED data recorded at 100 K with main interatomic distances indicated.

https://doi.org/10.1038/s41467-025-67333-z

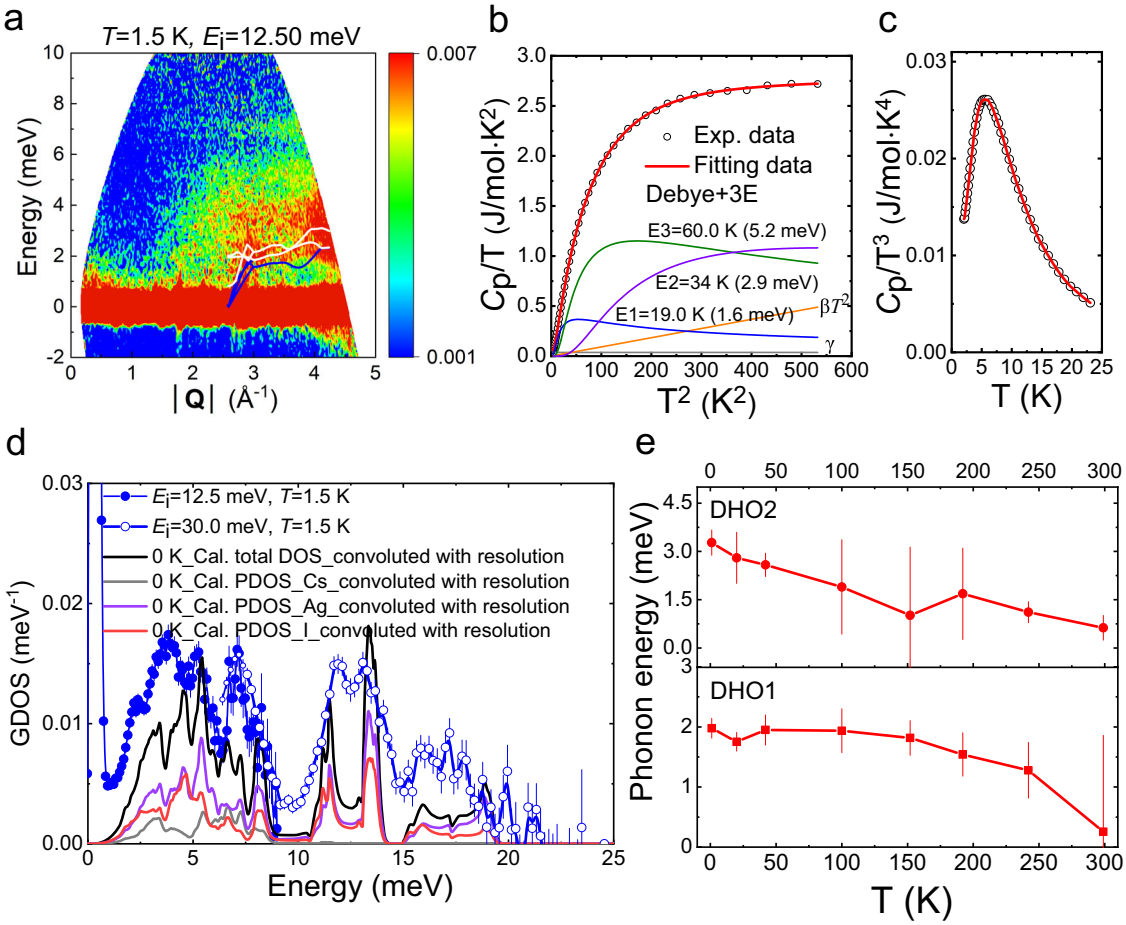

Fig. 4 | Temperature evolution of phonons in $CsAg_2I_3$. a Experimental $S(|\mathbf{Q}|, E)$ with $E_i = 12.50$ meV at $T = 1.5$ K. The blue and white solid lines denoted as the acoustic and optical phonons, respectively. **b** C_p/T vs. T^2 and **c** C_p/T^3 vs. T using the Debye-Einstein model. **d** Experimental GDOS determined with $E_i = 12.5$ meV (marked as the solid blue scatter points) and $E_i = 30.0$ meV (marked as the hollow blue scatter points) at $T = 1.5$ K. The calculated PDOS convoluted with a 0.6 meV resolution resulted in a solid black line. The calculated neutron-weighted partial phonon density of states for Cs (gray solid line), Ag (purple solid line), and I (pink solid line) atoms from 1.5–300 K. The experimental data for **e** temperature-dependent phonon modes of DHO1 and DHO2. The lines here are guides to the eye. Error bars represent standard deviations.

Additionally, we conducted a fitting analysis of the low-temperature C_p using the Debye-Einstein model. Detailed discussions of the fitting process and the Debye-Einstein model can be found in the referenced study[13]. The C_p/T versus T^2 plot in Fig. 4b illustrates a well-fitted profile, indicating three localized low-energy Einstein modes, with values E1 = 19.0 K (1.6 meV), E2 = 34.0 K (2.9 meV), and E3 = 60.0 K (5.2 meV). Importantly, these Einstein modes derived from C_p are also consistent with the INS findings obtained using high incident energy $E_i = 30.0$ meV and high-resolution $E_i = 12.5$ meV, further supporting the presence of low-energy optical modes in $CsAg_2I_3$. Figure 4c displays the excellent fitting profile of C_p/T^3 vs. T plot with Debye and three Einstein modes from 2 to 23 K. Notably, a distinct Boson peak is observed in the C_p/T^3 vs. T plot, revealing the presence of low-energy excitations[13].

To investigate the temperature dependence of low-energy phonons, we analyzed the constant-momentum spectra at $|\mathbf{Q}| = (3.2 \pm 0.1)$ Å^{-1} (as displayed in Fig. 4a), where the low-energy phonon signal is prominent. These constant $|\mathbf{Q}|$ spectra (Fig. S12) were fitted using a combination of functions: four damped harmonic oscillator (DHO) functions[33], a delta function for the elastic line (convoluted with a Gaussian-shaped resolution of 0.6 meV full-width at half-maximum, FWHM), and a background term. The four DHO components, labeled DHO1 to DHO4 in ascending energy, were used to characterize the phonon modes. The analysis revealed that the characteristic energies of DHO1 and DHO2 undergo continuous softening of the low-energy phonon peaks (Fig. 4e). Specifically, DHO1 and DHO2, with initial energies of 2 and 3.3 meV at 1.5 K, respectively, develop into overdamped phonons as temperature approaches 300 K. These low-energy modes can be viewed as soft phonons, which are closely associated with the displacive phase transition, such as superionic transitions[60]. The appearance of soft phonons in $CsAg_2I_3$ is likely linked to the structural transition from *Pnma* to *Cmcm* around 300 K. Besides, the characteristic energies of the high-energy optical phonons, referred as DHO3 and DHO4, exhibit a phonon softening behavior but without fully softening (Fig. S13) as observed in DHO1 and DHO2. Therefore, the presence of soft phonons and phonon softening in $CsAg_2I_3$ underscores its intrinsically strong anharmonic feature, contributing to its exceptionally low κ_L.

Microscopic mechanisms of ultralow glass-like κ_L

To better understand thermal transport in crystalline $CsAg_2I_3$ with space groups *Pnma* and *Cmcm*, we calculated κ_L using the unified theory of thermal transport[14], incorporating both population κ_L^P and diffuson contributions κ_L^C, as shown in Fig. 5a. It is worth noting that the calculated κ_L of the $CsCu_2I_3$ compound was reported[61] while this paper was in preparation, therefore, we focus here only on the theoretical study of the $CsAg_2I_3$ compound. When both 3-phonon (3 ph)

https://doi.org/10.1038/s41467-025-67333-z

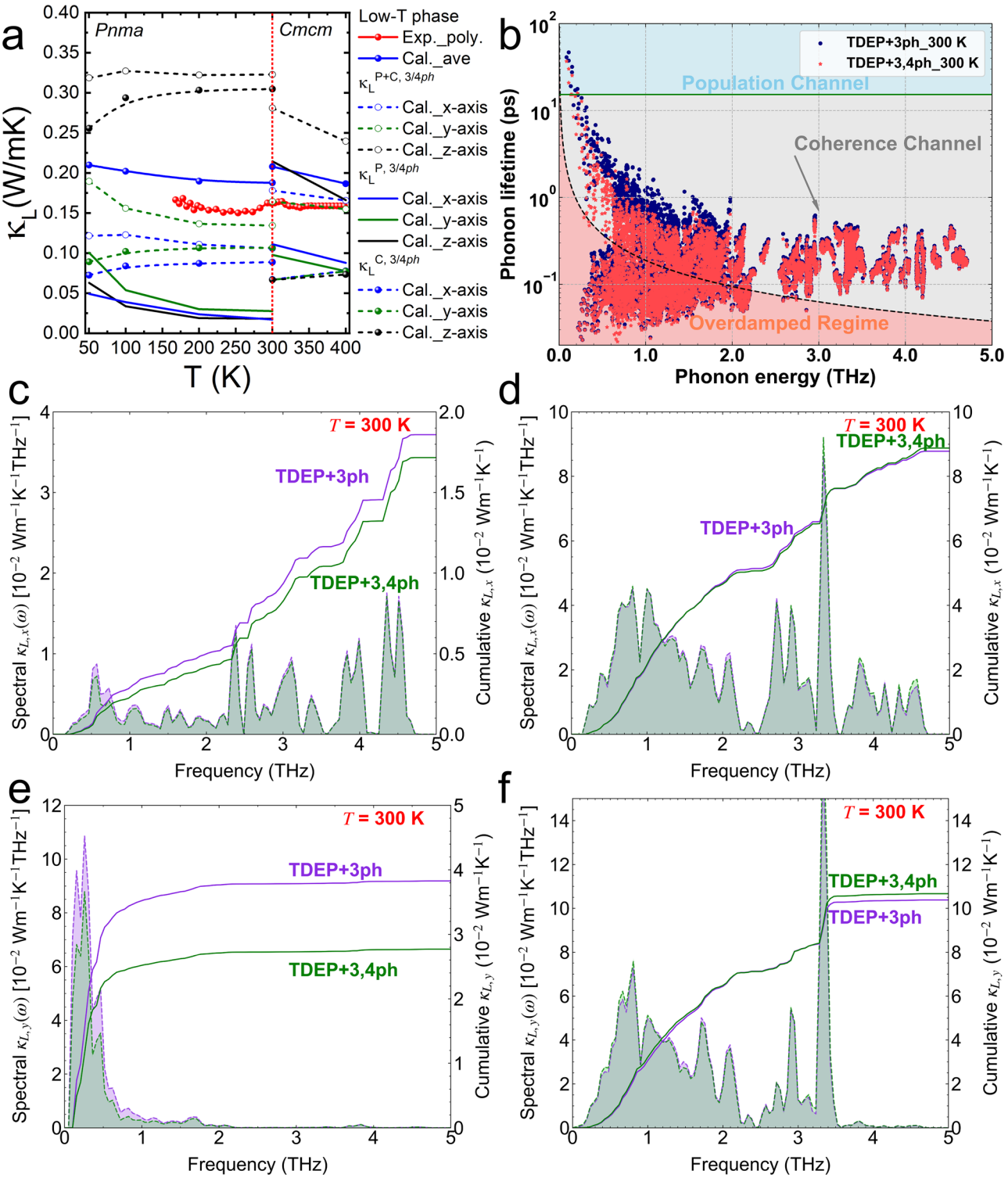

Fig. 5 | Phonon transport properties of $CsAg_2I_3$. a The calculated axis-dependent κ_L, including both population κ_L^P and coherence κ_L^C contributions, for crystalline $CsAg_2I_3$ with space group of *Pnma* and *Cmcm*, respectively. Since our experimental κ_L was measured in polycrystalline $CsAg_2I_3$, the averaged total thermal conductivity $\kappa_{L,ave}^{P+C}$ was computed for a fair comparison and shows good agreement with the experimental data. **b** The calculated phonon lifetime as a function of phonon frequency at $T = 300$ K, accounting for 3-phonon processes and both 3- and 4-phonon processes, respectively. The solid green line represents the Wigner limit in time[14], while the black dashed line indicates the Ioffe-Regel limit in time[34]. **c**,**d** The calculated spectral and cumulative population and diffuson thermal conductivity $\kappa_L^{P/C}(\Omega)/\kappa_L^{P/C}$ along the x- axis at $T = 300$ K, considering 3 ph and both 3- and 4 ph scattering processes, respectively. **e**, **f** The same as c-d, but for spectral and cumulative population and diffuson thermal conductivity $\kappa_L^{P/C}(\Omega)/\kappa_L^{P/C}$, along the y-axis.

and 4-phonon (4 ph) scattering processes are considered, the κ_L^C significantly dominates the total κ_L along all crystallographic axes. We predict a room-temperature κ_L^C of 0.09 W/m·K along the x-axis (0.11 and 0.30 W/m·K along the y- and z-axes, respectively), while the corresponding κ_L^P values are 0.02 W/m·K along the x-axis (0.03 and 0.02 W/m·K along the y- and z-axes, respectively) (see Fig. 5a).

Interestingly, even when considering both phonon and diffuson channels, we observe an exceptionally low total κ_L of 0.11 and 0.13 W/m·K

along the x-axis and y-axis, respectively, which is comparable to the experimentally recorded ultralow κ_L of 0.1 W/m·K in crystalline $Bi_4O_4SeCl_2$[12]. To validate our predicted κ_L, we averaged the computed total κ_L across all crystallographic orientations and compared it with our experimentally measured κ_L for the polycrystalline $CsAg_2I_3$ sample. From Fig. 5a, we observe that the comparison of κ_L between experiment and theory shows good agreement, although the theoretical values are slightly higher than the experimental measurements.

We next examine the glass-like behavior observed in both the experimentally measured and theoretically predicted κ_L, as illustrated in Fig. 5a. Notably, both the experimentally measured and theoretically predicted κ_L exhibit temperature-independent behavior over the range of 170–400 K. This temperature-independent behavior of κ_L has also been observed in cubic tetrahedrite $Cu_{12}Sb_4S_{13}$[15], although crystalline $CsAg_2I_3$ exhibits even lower thermal conductivity. Structural complexity can enhance thermal transport in materials with ultralow thermal conductivity[14] and may cause κ_L to exhibit positive temperature dependence[13] due to the dominant role of the diffuson channel[14]. The structural complexity of $CsAg_2I_3$, with 12(24) atoms per primitive cell (moderate complexity), may represent a critical threshold to suppress lattice κ_L to an ultralow limit.

To gain deeper insight into the microscopic mechanisms of thermal transport in crystalline $CsAg_2I_3$, we calculated both the phonon lifetimes and axis-dependent group velocities, as illustrated in Fig. 5b and Fig. S14, respectively. In Fig. 5b, most phonons have lifetimes shorter than the Wigner limit in time[34], highlighting the dominant role of diffuson contribution in the thermal transport of $CsAg_2I_3$, as shown in Fig. 5a. Notably, another eye-catching characteristic is that most phonon lifetimes approach the Ioffe-Regel limit[62], particularly for phonons with frequencies between 0.2–2.2 THz (approximated 1-9 meV, see Fig. 5b), indicating the strong lattice anharmonicity and main contributor to ultralow κ_L in $CsAg_2I_3$.

Combined with the structural complexity in crystalline $CsAg_2I_3$, the observation of strong anharmonicity further underscores the minor contribution of the particle-like phonon channel to the total κ_L. Additionally, from Fig. S14, we observe low v_g in crystalline $CsAg_2I_3$. Specifically, the highest v_g are 2200 m/s along the x-axis (1800 and 1200 m/s along the y- and z-axes, respectively). These low v_g further suppress phonon thermal transport in crystalline $CsAg_2I_3$, consistent with observations reported in the perovskites[50,63]. This unique characteristics of v_g leads to distinct features in the spectral κ_L^P along different crystallographic orientations, as shown in Fig. 5c, e and Fig. S15a.

For instance, the spectral κ_L^P along the x-axis is predominantly contributed by phonons with frequencies ranging from 0 to 4.6 THz (approximated 0-19 meV), whereas the κ_L^P along y- and z-axes is mainly contributed by phonons with frequencies below 1 THz (approximated 4 meV). In contrast, the spectral κ_L^C along all crystallographic orientations is contributed by all phonons, unaffected by the material's structure, due to its diffuson characteristics, as shown in Fig. 5d, f and Fig. S15b. By carefully comparing the atomic participation ratio (APR) (see Fig. S16), phonon lifetimes (see Fig. 5b), and spectral κ_L^P (see Fig. 5c, e and S15a), we find that the strong anharmonicity primarily originates from the I atoms. Notably, the atom-resolved PDOS (see Fig. S17) confirms that the low-energy phonon modes are primarily governed by the I-related atoms, further corroborating the large atomic vibration observed in the structural analysis. Additionally, the flattening modes associated with Cs atoms contribute significantly to phonon scattering rates. A similar phenomenon has also been observed in perovskites[50] and tetrahedrites[15]. Overall, the combination of weak bonding (low v_g) and strong anharmonicity results in the record-low thermal conductivity observed in crystalline $CsAg_2I_3$. Finally, from Fig. 5a, we observe a distinct difference in the phonon and coherence contributions to the total thermal conductivity between the *Pnma* and *Cmcm* phases. In the *Cmcm* phase, phonons contribute significantly to the total thermal conductivity, whereas in the *Pnma* phase, coherence effects dominate. This disparity can be attributed to structural complexity: the *Pnma* phase contains 24 atoms per unit cell, while the *Cmcm* phase contains only 12. The increased structural complexity in *Pnma* suppresses particle-like phonon transport and enhances diffuson contributions to thermal transport[14,34].

In summary, informed by the classical Slack model and a unified perspective on minimum κ_L, we derived a simple yet powerful universal descriptor, $n^{-\frac{2}{3}}(v/1000)^3$, for rapidly identifying crystalline materials exhibiting ULG-type κ_L. To avoid the time- and resource-intensive requirement of experimentally or theoretically determining v, we built a global database of υ for inorganic crystalline materials using high-throughput calculations and machine-learning methods, thereby accelerating the discovery of materials with targeted thermal transport properties. Guided by the universal descriptor and established global v database, we identified the CsA_2I_3 (A = Ag, Cu) halide family as a promising materials system, including the compounds $CsAg_2I_3$ and $CsCu_2I_3$. We synthesized polycrystals and characterized their thermal conductivities, which displayed record ULG-type κ_L of 0.15–0.20 W/m·K in the temperature of 170–523 K. To investigate the microscopic relationships between crystal structure, vibrational properties, and phonon transport, we further conducted in-depth PXRD, electron diffraction, INS, and unified theory to a representative compound $CsAg_2I_3$.

The temperature-dependent PXRD confirmed the orthorhombic crystal structure of $CsAg_2I_3$ characterized by the *Pnma* space group below 300 K and revealed a structural transition to *Bbmm*/*Cmcm* space group above 300 K. This compound, with a moderate complexity of $n = 24$ for *Pnma* and $n = 12$ for *Cmcm*, can be viewed as consisting of a building unit $[Ag_2I_3]^-$ anionic chains (1D character), along with Cs^+ playing the role of counter-cations. The structural analysis emphasizes the key role of iodine vibration and weak Ag-I bonds in the thermal conductivity of the low-temperature form, resulting in extremely low v and large anharmonicity. Moreover, our temperature-dependent INS experiments revealed the presence of soft optical phonons located at ~2 meV as well as a phonon softening feature at elevated temperatures, further supporting a strong anharmonic feature. Our unified theory of thermal transport also highlights the dominant diffuson thermal transport properties, and the coexistence of extremely low κ_L^C and κ_L^P in $CsAg_2I_3$. These features, enabled by moderate complexity and strong anharmonicity, are responsible for ULG-type κ_L of this material. Thus, the discovery of record-low ULG-type κ_L in the CsA_2I_3 (A = Ag, Cu) halide system provides compelling evidence for the utility of our universal descriptor, high-throughput methodology, and universal machine-learning potentials in identifying crystalline materials exhibiting ULG-type κ_L. The applicability and versatility of our descriptor are anticipated to bridge the gap in evaluating ultralow κ_L in crystalline inorganic materials across a broad temperature range. By offering a low-cost and easily deployable approach for both experimentalists and theorists, this work enables accelerated discovery of thermally functional materials for diverse applications.

Methods

Synthesis

The metal halide compounds $CsAg_2I_3$ and $CsCu_2I_3$ were prepared using stoichiometric amounts of precursors CsI (powder, 99.9%), AgI (powder, 99.9%), and CuI (powder, 99.9%). The mixtures of precursors were ground into fine powders in an Ar-filled glove box. The resulting powders were then cold-pressed into pellets and placed in carbon-coated silica tubes. These tubes were subsequently evacuated and sealed under a vacuum of ~10^{-3} Pa. The sealed tubes were heated to 623 K over a period of 7 h and held at this temperature for an additional 24 h, followed by cooling down within 7 h. The obtained ingots of $CsAg_2I_3$ and $CsCu_2I_3$ were ground into fine powders and loaded into a 10 mm graphite die, followed by densification through spark plasma sintering (SPS) at 473 and 523 K, respectively, for 5 min under an

applied pressure of 64 MPa. The resultant SPS-ed samples were confirmed to be a highly densified pellet with a 98% of the theoretical density.

X-ray diffraction

Temperature-dependent high-resolution PXRD of the synthesized SPS-ed $CsAg_2I_3$ powder were conducted from 250 to 320 K utilizing a Smartlab 9 kW Phenix chamber system equipped with Cu $K_{\alpha1}$ radiation ($\lambda = 1.5406$ Å) and Johansson Ge (111) monochromator. High-resolution PXRD data of the synthesized SPS-ed $CsCu_2I_3$ powders were recorded at 300 K using a Bruker D8 Advance Vario 1 two-circle diffractometer ($\theta - 2\theta$, Bragg–Brentano mode) equipped with Cu $K_{\alpha1}$ radiation ($\lambda = 1.5406$ Å) and a Ge (111) monochromator (Johansson type). Rietveld refinements were carried out using the FullProf[64] and WinPlotr[65] software packages, incorporating the refinement of parameters, such as zero-point shift, unit cell, peak shape, asymmetry, atomic coordinates, and B_{iso} values of each atoms.

3D electron diffraction and scanning electron microscopy

3D Electron Diffraction (3D ED)[66] is a technique that uses electron diffraction patterns collected from a single crystal to determine its crystal structure. For this study, precession-assisted 3D ED data were collected using a JEOL F200 transmission electron microscope at 200 kV, equipped with an ASI Cheetah M3 detector and a Nanomegas Digistar precession unit. A $CsAg_2I_3$ pellet was ground in ethanol with an agate mortar, and a drop of the resulting suspension was deposited onto a holey carbon membrane on a Cu mesh grid. 3D ED data were recorded at 100 K using a GATAN ELSA tomography holder and the Instamatic program[67], with a precession angle of 1.25° and a tilt step of approximately 2° between patterns. Data processing was performed with PETS2[68], and structure refinements were carried out in Jana2020[69], accounting for both dynamical diffraction effects and electron beam precession. The refined structural parameters of $CsAg_2I_3$ are summarized in Table S8. Scanning electron micrographs and electron energy dispersive spectroscopy (EDS) analyses of samples were performed using a JEOL JSM-7200F-SEM equipped with an EDX X-Flash Bruker detector.

Heat capacity and thermal conductivity measurements

The thermal conductivity (κ) was calculated employing the formula $\kappa = \rho C_p d$. The wide-range thermal diffusivity (d) of the $CsAg_2I_3$ sample was measured using a Netzsch LFA 467 Hyper flash system under a nitrogen atmosphere from 170 to 400 K, while high-temperature d of the $CsCu_2I_3$ samples were conducted utilizing a Netzsch LFA 457 laser flash system under a nitrogen atmosphere from 300 to 523 K. The density (ρ) was determined via the Archimedes method. C_p measurement of the $CsAg_2I_3$ sample were conducted in the temperature range of 2 to 350 K using a conventional relaxation method with the dedicated ^{4}He option of the PPMS.

Sound velocity measurements

The pulse-echo method was employed to measure the longitudinal and transverse sound velocities of the $CsAg_2I_3$ sample at 300 K. A small quantity of grease was applied to ensure effective contact between the sample and the piezoelectric transducers.

Inelastic neutron scattering

Inelastic neutron scattering experiments were conducted on a powder sample weighing ~10 g. The sample was measured at temperatures between 1.5 and 300 K using the thermal neutron time-of-flight spectrometer PANTHER at the Institut Laue Langevin in Grenoble, France. We employed nominal incident energies E_i of 30.0 meV to examine the full phonon spectrum and 12.5 meV to monitor low-energy phonons. We utilized a standard cryostat, with the powder sample contained in an aluminum sample holder. The acquisition periods varied from 1 to 2 hours, depending on E_i and temperature, which influenced the inelastic intensity.

The evolution of the low-energy phonons was recorded during cooling from 300 K to 1.5 using an $E_i = 12.5$ meV. An acquisition period of 10 min led to a temperature difference of 5 K or less between spectra. To ensure accurate data analysis, we performed additional measurements on empty sample holders, the sample environments, and vanadium. These measurements were essential for standardizing our data correction procedure and converting the corrected signal to the dynamic structure factor $S(|\mathbf{Q}|, E)$ and the GDOS $g^{(n)}(E)$. We utilized the Mantid software package for the correction and conversion computing[70].

For a given polyatomic material, GDOS can be approximated from the atomic partial phonon density of states ($g_i^{(n)}(E)$) of element i as Eq. (5)[60]:

$$g^{(n)}(E) = \sum_i f_i \frac{\sigma_i}{m_i} g_i(E) \exp(-2W_i) \tag{5}$$

Where i, f_i, σ_i, m_i, and W_i denote the different elements, atomic concentration, neutron total cross-section, mass, and Debye-Waller factor of element i, respectively. The values of $\frac{\sigma_i}{m_i}$ for Cs, Ag, and I are 0.03, 0.046, and 0.03 barn/amu.

Density functional theory calculations

In this work, all the ab initio calculations for crystalline $CsAg_2I_3$ were conducted using density functional theory (DFT)[71], as implemented in the Vienna Ab initio Simulation Package (VASP)[72]. The projector-augmented wave (PAW)[73] pseudopotentials were utilized to explicitly treat the $5s^25p^66s^1$, $4d^{10}5s^1$ and $5s^25p^5$ electrons as valence states for Cs, Ag, and I atoms, respectively. For the exchange-correlation functional in all DFT calculations, we employed the revised Perdew-Burke-Ernzerhof (PBE) version for solids, i.e., PBEsol functional[74], within the generalized gradient approximation (GGA) framework[75]. In both structural relaxation and self-consistent DFT calculations, tight convergence criteria were applied, with force convergence set to 10^{-5} eV·Å^{-1} and energy convergence to 10^{-8} eV. For crystalline $CsAg_2I_3$ with a space group of *Pnma*, a kinetic energy cutoff of 600 eV and a Γ-centered 8 × 10 × 8 Monkhorst-Pack k-mesh were used to sample the Brillouin zone in the primitive cell, which contains 24 atoms. The resulting fully relaxed lattice constants are $a = 13.9250$ Å, $b = 5.8845$ Å and $c = 11.3099$ Å. Similarly, for crystalline $CsAg_2I_3$ with a space group of *Cmcm*, the same kinetic energy cutoff and a Γ-centered 10 × 10 × 10 Monkhorst-Pack k-mesh were employed to sample the Brillouin zone in the primitive cell containing 12 atoms. The fully optimized primitive-cell lattice constants are $a = b = 8.9727$ Å and $c = 5.8862$ Å. For the corresponding conventional unit cell, the lattice constants are $a = 11.2991$ Å, $b = 13.9416$ Å, and $c = 5.8862$ Å.

Effective harmonic force constants extraction

To obtain the effective harmonic phonon frequency at finite temperatures, the temperature-dependent effective potential (TDEP) method[76] was used to fit first-principles forces to an effective Hamiltonian (H),

$$H = U_0 + \sum_i \frac{\boldsymbol{P}_i^2}{2m_i} + \frac{1}{2}\sum_{ij\alpha\beta} \Phi_{ij}^{\alpha\beta} u_i^\alpha u_j^\beta, \tag{6}$$

where U_0 denotes the potential energy, i and j denote the atomic indeces, p_i denotes the momentum associated with atom i, m_i denotes atomic mass, u_i denotes atomic displacment. $\Phi_{ij}^{\alpha\beta}$ denotes the effective harmonic interatomic force constants (IFCs), associated with the Cartesian indices α and β.

To prepare the finite-temperature displacement-force dataset for IFCs extraction, stochastic sampling of the canonical ensemble was

employed to generate perturbed supercells[77,78], followed by precise self-consistent DFT calculations to determine the forces on all atoms. The Cartesian displacement (u_i^α) is normally distributed around the mean thermal dispacement and is expressed as

$$u_i^\alpha = \sum_q e_q^{i\alpha} \left\langle A_{iq} \right\rangle \sqrt{-2\ln\zeta_1}\sin(2\pi\zeta_2) \tag{7}$$

with the thermal amplitude $\langle A_{iq}\rangle$ given as[77–79]

$$\left\langle A_{iq} \right\rangle = \sqrt{\frac{\hbar(2n_q^0+1)}{2m_i\omega_q}}, \tag{8}$$

where q represents the phonon mode, acting as a composite index that combines the wavevector $\mathbf{q}$ and phonon branch s, e_q represents the eigenvector, ζ_1 and ζ_2 represent stochastically sampled numbers between 0 and 1, $\hbar$, n_q and ω_q represent the Planck constants, the occupation number following the Bose-Einstein distribution and the phonon frequency, respectively.

In this work, a 1 × 2 × 2 supercell containing 96 atoms of crystalline $CsAg_2I_3$ with space group of *Pnma* was used to perform calculations iteratively, starting with 500 thermally perturbed snapshots. The resulting 500 atomic configurations were then used to generate the displacement-force dataset through precise DFT calculations with a Γ-centered 4 × 4 × 4 Monkhorst-Pack k-point density grid. Each iteration involves key procedures, including computing phonon normal modes, generating perturbed snapshots, calculating precise DFT forces, and fitting effective IFCs. To ensure the convergence of finite-temperature IFCs, the final iteration at each temperature (50, 100, 200, 300, and 400 K) was performed using 1500 snapshots.

For the crystalline $CsAg_2I_3$ with space group of *Cmcm*, a 2 × 2 × 2 supercell containing 96 atoms was used for the iterative calculations of effective IFCs. Similarly, the iteration was initiated with 500 thermally perturbed snapshots generated from zero-K phonon dispersions. Precise forces were obtained through self-consistent DFT calculation using a Γ-centered 4 × 4 × 4 Monkhorst-Pack k-point density grid. The final iteration at each temperature (300 and 400 K) was conducted with 1500 snapshots to ensure the convergence of finite-temperature IFCs. In this study, the temperature-dependent effective potential calculations were performed using the ALAMODE package[80].

Effective anharmonic force constants extraction

Instead of the least-squares approach for extracting the effective harmonic interatomic force constants (IFCs), the Compressive Sensing Lattice Dynamics (CSLD) method[81] was employed to efficiently and accurately extract the anharmonic IFCs. The CSLD method efficiently identifies the physically significant terms from a large set of irreducible anharmonic IFCs using a limited displacement-force dataset[81]. To extract the effective anharmonic IFCs, we sampled a dataset consisting of 300 configurations, with each configuration containing up to 96 displacement-force pairs, from the previous harmonic canonical ensemble at finite temperatures[76,82]. Subsequently, the effective harmonic IFCs and the displacement-force dataset were used as an input to extract anharmonic IFCs up to the sixth order. The anharmonic IFCs of crystalline $CsAg_2I_3$ with both space groups *Pnma* and *Cmcm* were extracted using the least absolute shrinkage and selection operator (LASSO) technique[83], with real-space cutoff radii of 7.41 Å, 6.35 Å, 4.23 Å, and 3.17 Å for the cubic, quartic, quintic, and septic IFCs, respectively. In this work, the IFCs fitting process was performed using the ALAMODE package[80,81,84].

Anharmonic phonon scattering rates

With the effective interatomic force constants (IFCs) available and using the Fermi's golden rule[85], the phonon scattering rates for three-phonon (3 ph) Γ_q^{3ph} and four-phonon (4 ph) Γ_q^{4ph} processes under the single-mode relaxation time approximation (SMRTA) are expressed as[15,85]

$$\Gamma_q^{3ph} = \sum_{q'q''}\left\{\frac{1}{2}\left(1+n_{q'}^0+n_{q''}^0\right)\mathscr{L}_- + \left(n_{q'}^0-n_{q''}^0\right)\mathscr{L}_+\right\}, \tag{9}$$

$$\Gamma_q^{4ph} = \sum_{q'q''q'''}\left\{\frac{1}{6}\left(\frac{n_{q'}^0 n_{q''}^0 n_{q'''}^0}{n_q^0}\right)\mathscr{L}_{--} + \frac{1}{2}\left(\frac{\left(1+n_{q'}^0\right)n_{q''}^0 n_{q'''}^0}{n_q^0}\right)\mathscr{L}_{+-} + \frac{1}{2}\left(\frac{\left(1+n_{q'}^0\right)\left(1+n_{q''}^0\right)n_{q'''}^0}{n_q^0}\right)\mathscr{L}_{++}\right\}, \tag{10}$$

with

$$\mathscr{L}_\pm = \frac{\pi\hbar}{4N}\left|V^{(3)}(q,\pm q',-q'')\right|^2\Delta_\pm\frac{\delta\left(\Omega_q\pm\Omega_{q'}-\Omega_{q''}\right)}{\Omega_q\Omega_{q'}\Omega_{q''}}, \tag{11}$$

and

$$\mathscr{L}_{\pm\pm} = \frac{\pi\hbar^2}{8N^2}\left|V^{(4)}(q,\pm q',\pm q'',-q''')\right|^2\Delta_{\pm\pm}\frac{\delta\left(\Omega_q\pm\Omega_{q'}\pm\Omega_{q''}-\Omega_{q'''}\right)}{\Omega_q\Omega_{q'}\Omega_{q''}\Omega_{q'''}} \tag{12}$$

where Ω_q denotes the effective phonon frequency, $V^{(3)}(q,\pm q',-q'')$ and $V^{(4)}(q,\pm q',\pm q'',-q''')$ denote the reciprocal forms of 3rd- and 4th-order effective IFCs[86], i.e., the strength of the 3 ph and 4 ph scattering matrices, respectively. In 3 and 4 ph scattering processes, energy conservation is enforced using the delta function δ, while momentum conservation is imposed via the Kronecker delta Δ.

The extrinsic phonon-isotope scattering rate Γ_q^{iso} also plays a critical role in thermal transport and can be expressed as[87]

$$\Gamma_q^{iso} = \frac{\pi\Omega_q^2}{2N}\sum_{i\in u.c.} g(i)\left|e_q^*(i)\cdot e_{q'}(i)\right|^2\delta(\Omega-\Omega') \tag{13}$$

Where $g(i)$ denotes the Pearson deviation coefficient. Under the assumption of Matthiessen's rule, the total phonon scattering rate Γ_q for a specific mode q is expressed as

$$\Gamma_q = \Gamma_q^{3ph}+\Gamma_q^{4ph}+\Gamma_q^{iso} \tag{14}$$

The unified theory of thermal transport

Given the strong anharmonicity and structural complexity of crystalline $CsAg_2I_3$, the unified theory of thermal transport proposed by Michelle et al.[14,34], which accounts for both κ_L^C and κ_L^P, was employed to calculate the total lattice thermal conductivity κ_L. Within the SMRTA framework, the unified theory of thermal transport is expressed as[14,34]

$$\kappa_L^{P/C} = \frac{\hbar^2}{k_B T^2 VN}\sum_{\boldsymbol{q}}\sum_{s,s'}\frac{\Omega_{\boldsymbol{q}s}+\Omega_{\boldsymbol{q}s'}}{2}\cdot\nu_{\boldsymbol{q}ss'}\bigotimes\nu_{\boldsymbol{q}s's}\cdot\frac{\Omega_{\boldsymbol{q}s}n_{\boldsymbol{q}s}\left(n_{\boldsymbol{q}s}+1\right)+\Omega_{\boldsymbol{q}s'}n_{\boldsymbol{q}s'}\left(n_{\boldsymbol{q}s'}+1\right)}{4\left(\Omega_{\boldsymbol{q}s}+\Omega_{\boldsymbol{q}s'}\right)^2+\left(\Gamma_{\boldsymbol{q}s}+\Gamma_{\boldsymbol{q}s'}\right)^2}\cdot\left(\Gamma_{\boldsymbol{q}s}+\Gamma_{\boldsymbol{q}s'}\right), \tag{15}$$

where k_B, T, V, and N are the Boltzmann constant, the cell volume, the absolute temperature and the number of sampled phonon wave vectors, ν is the inter- and intra-band group velocity matrix and can be

expressed as[88]

$$\nu_{qss'} = \frac{\langle e_{qs} \left| \frac{\partial D(q)}{\partial q} \right| e_{qs'} \rangle}{2\sqrt{\Omega_{qs}\Omega_{qs'}}} \quad (16)$$

Where $D(q)$ denotes the dynamical matrix. The interband term ($s = s\prime$) results in diagonal terms of heat flux operators and contributing to κ_L^P. In contrast, the intraband term ($s \neq s'$) gives rise to off-diagonal terms of heat flux operators and contributing to κ_L^c. To calculate the total lattice thermla conductivity κ_L of crystalline $CsAg_2I_3$ with space group of *Pnma*(*Cmcm*), which contains 24(12) atoms in the primitive cell, a q mesh of 8 × 8 × 8 (12 × 12 × 12) was used for both 3 ph and 4 ph scattering processes, with a scalebroadening parameter of 0.1(0.2). The parameters chosen for Eq.(15) were thoroughly tested for the convergence and yield well-converged results. In this work, lattice thermal conductivity calculations, including population and coherence contributions, were performed using the ShengBTE[89] and FourPhonon[86] packages, along with our in-house code[49,50].

The high-throughput calculation and universal machine-learning force field: MACE

MACE is an equivariant message passing neural network potential, using higher order messages combined with Atomic Cluster Expansion (ACE), a method for deriving an efficient basis to represent functions of atomic neighborhoods. Note that the version of MACE used in this work is the MACE-MP-0 (medium) (https://github.com/ACEsuit/mace-foundations), as implemented in the atomate2 package[90].

Data availability

The data supporting the construction of a universal descriptor of this study are all available in the main text and supplementary information. The high-throughput calculation of sound velocity was obtained using MACE[28], and the original data generated in this study is available in the repository: https://github.com/leslie-zheng/High-throughput-group-velocity-calculation. The raw data of the inelastic neutron scattering experiments is available in the repository: https://doi.org/10.5291/ILL-DATA.7-01-592.

Code availability

The open-source codes can be found as following: Alamode is available at https://github.com/ttadano/alamode, ShengBTE is available at https://www.shengbte.org, and FOURPHONON is available at https://github.com/FourPhonon/FourPhonon. Atomate2 is available at https://github.com/materialsproject/atomate2. MACE is available at https://github.com/ACEsuit/mace. The in-house codes will be available from the corresponding authors upon reasonable request.

References

1. Bell, L. E. Cooling, heating, generating power, and recovering waste heat with thermoelectric systems. *Science* **321**, 1457–1461 (2008).
2. Padture, N. P., Gell, M. & Jordan, E. H. Thermal barrier coatings for gas-turbine engine applications. *Science* **296**, 280–284 (2002).
3. Qian, X., Zhou, J. & Chen, G. Phonon-engineered extreme thermal conductivity materials. *Nat. Mater.* **20**, 1188–1202 (2021).
4. Shi, Y., Assoud, A., Ponou, S., Lidin, S. & Kleinke, H. A new material with a composite crystal structure causing ultralow thermal conductivity and outstanding thermoelectric properties: $Tl_2Ag_{12}Te_{7+\delta}$. *J. Am. Chem. Soc.* **140**, 8578–8585 (2018).
5. Peng, W., Petretto, G., Rignanese, G.-M., Hautier, G. & Zevalkink, A. An unlikely route to low lattice thermal conductivity: small atoms in a simple layered structure. *Joule* **2**, 1879–1893 (2018).
6. Christensen, M. et al. Avoided crossing of rattler modes in thermoelectric materials. *Nat. Mater.* **7**, 811–815 (2008).
7. Li, C. W. et al. Orbitally driven giant phonon anharmonicity in SnSe. *Nat. Phys.* **11**, 1063–1069 (2015).
8. Skelton, J. M. et al. Anharmonicity in the high-temperature Cmcm phase of SnSe: soft modes and three-phonon interactions. *Phys. Rev. Lett.* **117**, 075502 (2016).
9. Pal, K., He, J. & Wolverton, C. Bonding hierarchy gives rise to high thermoelectric performance in layered Zintl compound BaAu2P4. *Chem. Mater.* **30**, 7760–7768 (2018).
10. Mukhopadhyay, S. et al. Two-channel model for ultralow thermal conductivity of crystalline Tl_3VSe_4. *Science* **360**, 1455–1458 (2018).
11. Acharyya, P. et al. Glassy thermal conductivity in $Cs_3Bi_2I_6Cl_3$ single crystal. *Nat. Commun.* **13**, 5053 (2022).
12. Gibson, Q. D. et al. Low thermal conductivity in a modular inorganic material with bonding anisotropy and mismatch. *Science* **373**, 1017–1022 (2021).
13. Shen, X. et al. Amorphous-like ultralow thermal transport in crystalline argyrodite Cu_7PS_6. *Adv. Sci.* **11**, 2400258 (2024).
14. Simoncelli, M., Marzari, N. & Mauri, F. Unified theory of thermal transport in crystals and glasses. *Nat. Phys.* **15**, 809–813 (2019).
15. Xia, Y., Ozoliņš, V. & Wolverton, C. Microscopic mechanisms of glasslike lattice thermal transport in cubic $Cu_{12}Sb_4S_{13}$ tetrahedrites. *Phys. Rev. Lett.* **125**, 085901 (2020).
16. Hanus, R. et al. Uncovering design principles for amorphous-like heat conduction using two-channel lattice dynamics. *Mater. Today Phys.* **18**, 100344 (2021).
17. Xia, Z. et al. Realizing intrinsically ultralow and glass-like thermal transport via chemical bonding engineering. *Adv. Sci.* **12**, 2417292 (2025).
18. Li, F. et al. Long-range anion correlations mediating dynamic anharmonicity and contributing to glassy thermal conductivity in well-ordered $K_2Ag_4Se_3$. *Small* **21**, 2409524 (2025).
19. Zheng, J. et al. Effects of high-order anharmonicity on anomalous lattice dynamics and thermal transport in fully filled skutterudite $YbFe_4Sb_{12}$. *Phys. Rev. Mater.* **6**, 093801 (2022).
20. Yang, J., Jain, A. & Ong, W.-L. Inter-channel conversion between population-/coherence-channel dictates thermal transport in MAPbI3 crystals. *Mater. Today Phys.* **28**, 100892 (2022).
21. Knoop, F., Purcell, T. A. R., Scheffler, M. & Carbogno, C. Anharmonicity in thermal insulators: an analysis from first principles. *Phys. Rev. Lett.* **130**, 236301 (2023).
22. Zeng, Z. et al. Pushing thermal conductivity to its lower limit in crystals with simple structures. *Nat. Commun.* **15**, 3007 (2024).
23. Slack G. A. The Thermal Conductivity of Nonmetallic Crystals. In: Ehrenreich H., Seitz F., Turnbull D. (eds). *Solid State Physics*, vol. 34, 1-71 (Academic Press, 1979).
24. Callaway, J. Model for lattice thermal conductivity at low temperatures. *Phys. Rev.* **113**, 1046–1051 (1959).
25. Xia, Y. et al. A unified understanding of minimum lattice thermal conductivity. *Proc. Natl. Acad. Sci. USA* **120**, e2302541120 (2023).
26. Wang, X. et al. An interpretable formula for lattice thermal conductivity of crystals. *Mater. Today Phys.* **48**, 101549 (2024).
27. Agne, M. T., Hanus, R. & Snyder, G. J. Minimum thermal conductivity in the context of diffuson-mediated thermal transport. *Energy Environ. Sci.* **11**, 609–616 (2018).
28. Batatia, I. et al. A foundation model for atomistic materials chemistry. *J. Chem. Phys.* **163**, 184110 (2025).
29. Chen, C. & Ong, S. P. A universal graph deep learning interatomic potential for the periodic table. *Nat. Comput. Sci.* **2**, 718–728 (2022).
30. Deng, B. et al. CHGNet as a pretrained universal neural network potential for charge-informed atomistic modelling. *Nat. Mach. Intell.* **5**, 1031–1041 (2023).
31. H. Yang. et al. MatterSim: a deep learning atomistic model across elements, temperatures and pressures. *arXiv* 2024, https://arxiv.org/abs/2405.04967.

32. Jain, A. et al. Commentary: the materials project: a materials genome approach to accelerating materials innovation. *APL Mater.* **1**, 011002 (2013).
33. Li, W. et al. Low sound velocity contributing to the high thermoelectric performance of Ag_8SnSe_6. *Adv. Sci.* **3**, 1600196 (2016).
34. Simoncelli, M., Marzari, N. & Mauri, F. Wigner formulation of thermal transport in solids. *Phys. Rev. X* **12**, 041011 (2022).
35. Peierls, R. Zur kinetischen Theorie der Wärmeleitung in Kristallen. *Ann. der Phys.* **395**, 1055–1101 (1929).
36. Slack, G. A., Tanzilli, R. A., Pohl, R. O. & Vandersande, J. W. The intrinsic thermal conductivity of AIN. *J. Phys. Chem. Solids* **48**, 641–647 (1987).
37. Ward, A., Broido, D. A., Stewart, D. A. & Deinzer, G. Ab initio theory of the lattice thermal conductivity in diamond. *Phys. Rev. B* **80**, 125203 (2009).
38. Steigmeier, E. F. & Kudman, I. Acoustical-optical phonon scattering in Ge, Si, and III-V compounds. *Phys. Rev.* **141**, 767–774 (1966).
39. Xiao, Y. et al. Origin of low thermal conductivity in SnSe. *Phys. Rev. B* **94**, 125203 (2016).
40. Zhang, J. et al. Direct observation of one-dimensional disordered diffusion channel in a chain-like thermoelectric with ultralow thermal conductivity. *Nat. Commun.* **12**, 6709 (2021).
41. Misra, S. et al. Reduced phase space of heat-carrying acoustic phonons in single-crystalline InTe. *Phys. Rev. Res.* **2**, 043371 (2020).
42. Zhu, J. et al. Vacancies tailoring lattice anharmonicity of Zintl-type thermoelectrics. *Nat. Commun.* **15**, 2618 (2024).
43. Acharyya, P. et al. Extended antibonding states and phonon localization induce ultralow thermal conductivity in low dimensional metal halide. *Adv. Funct. Mater.* **33**, 2304607 (2023).
44. Li, J. et al. First-principles studies of atomic dynamics in tetrahedrite thermoelectrics. *APL Mater.* **4**, 104811 (2016).
45. Shen, X. et al. High-temperature structural and thermoelectric study of argyrodite Ag_8GeSe_6. *ACS Appl. Mater. Interfaces* **11**, 2168–2176 (2019).
46. Li, F. et al. Overdamped phonon diffusion and nontrivial electronic structure leading to a high thermoelectric figure of merit in KCu_5Se_3. *J. Am. Chem. Soc.* **145**, 14981–14993 (2023).
47. Morelli, D. T., Jovovic, V. & Heremans, J. P. Intrinsically minimal thermal conductivity in Cubic I-V-VI_2 semiconductors. *Phys. Rev. Lett.* **101**, 035901 (2008).
48. Slack, G. A. Nonmetallic crystals with high thermal conductivity. *J. Phys. Chem. Solids* **34**, 321–335 (1973).
49. Zheng, J. et al. Anharmonicity-induced phonon hardening and phonon transport enhancement in crystalline perovskite $BaZrO_3$. *Phys. Rev. B* **105**, 224303 (2022).
50. Zheng, J. et al. Unravelling ultralow thermal conductivity in perovskite $Cs_2AgBiBr_6$: dominant wave-like phonon tunnelling and strong anharmonicity. *npj Comput. Mater.* **10**, 30 (2024).
51. Anderson, O. L. A simplified method for calculating the debye temperature from elastic constants. *J. Phys. Chem. Solids* **24**, 909–917 (1963).
52. Lee, W. et al. Ultralow thermal conductivity in all-inorganic halide perovskites. *Proc. Natl. Acad. Sci.* **114**, 8693–8697 (2017).
53. Cheng, R., Wang, C., Ouyang, N., Shen, X. & Chen, Y. Strong crystalline thermal insulation induced by extended antibonding states. *Nat. Commun.* **16**, 7941 (2025).
54. Hull, S. & Berastegui, P. Crystal structures and ionic conductivities of ternary derivatives of the silver and copper monohalides—II: ordered phases within the $(AgX)_x$–$(MX)_{1-x}$ and $(CuX)_x$–$(MX)_{1-x}$ (M=K, Rb and Cs; X=Cl, Br and I) systems. *J. Solid State Chem.* **177**, 3156–3173 (2004).
55. Yao, M.-M. et al. Lead-Free Halide $CsAg_2I_3$ with 1D electronic structure and high stability for ultraviolet photodetector. *Adv. Funct. Mater.* **32**, 2202894 (2022).
56. Jouini N., Guen L., Tournoux M. Structure Cristalline De Cscu2i3. (Springer, 1980).
57. Acharyya, P. et al. Intrinsically ultralow thermal conductivity in Ruddlesden–Popper 2D perovskite $Cs_2PbI_2Cl_2$: localized anharmonic vibrations and dynamic octahedral distortions. *J. Am. Chem. Soc.* **142**, 15595–15603 (2020).
58. Bhui, A. et al. Intrinsically low thermal conductivity in the n-Type vacancy-ordered double perovskite Cs_2SnI_6: octahedral rotation and anharmonic rattling. *Chem. Mater.* **34**, 3301–3310 (2022).
59. Xie, H. et al. All-inorganic halide perovskites as potential thermoelectric materials: dynamic cation off-centering induces ultralow thermal conductivity. *J. Am. Chem. Soc.* **142**, 9553–9563 (2020).
60. Shen, X. et al. Soft phonon mode triggering fast Ag diffusion in superionic argyrodite Ag_8GeSe_6. *Small* **19**, 2305048 (2023).
61. Zheng J. et al. Wave-like tunneling of phonons dominates glass-like thermal transport in quasi-1D copper halide $CsCu_2I_3$. *arXiv* 2023. https://arxiv.org/abs/2310.13680
62. Ioffe A., Regel A. Non-crystalline, amorphous, and liquid electronic semiconductors. *Progress in Semiconductors*, 237-291 (Springer, 1960).
63. Elbaz, G. A. et al. Phonon speed, not scattering, differentiates thermal transport in lead halide perovskites. *Nano Lett.* **17**, 5734–5739 (2017).
64. Rodríguez-Carvajal, J. Recent advances in magnetic structure determination by neutron powder diffraction. *Phys. B: Condens. Matter* **192**, 55–69 (1993).
65. Roisnel, T. & Rodríquez-Carvajal, J. WinPLOTR: a windows tool for powder diffraction pattern analysis. *Mater. Sci. Forum* **378-381**, 118–123 (2001).
66. Gemmi, M. et al. 3D electron diffraction: the nanocrystallography revolution. *ACS Cent. Sci.* **5**, 1315–1329 (2019).
67. Smeets, S., Zou, X. & Wan, W. Serial electron crystallography for structure determination and phase analysis of nanocrystalline materials. *J. Appl. Crystallogr.* **51**, 1262–1273 (2018).
68. Palatinus, L. et al. Specifics of the data processing of precession electron diffraction tomography data and their implementation in the program PETS2.0. *Acta Crystallogr. Sect. B* **75**, 512–522 (2019).
69. Petříček V., Palatinus L., Plášil J., Dušek M. Jana2020 – a new version of the crystallographic computing system Jana. *Crystal. Mater.* **238**, 271–282 (2023).
70. Arnold, O. et al. Mantid—Data analysis and visualization package for neutron scattering and μ SR experiments. *Nucl. Instrum. Methods Phys. Res. Sect. A Accelerator Spectrometers Detect. Assoc. Equip.* **764**, 156–166 (2014).
71. Hohenberg, P. & Kohn, W. Inhomogeneous electron gas. *Phys. Rev.* **136**, B864–B871 (1964).
72. Kresse, G. & Furthmüller, J. Efficient iterative schemes for ab initio total-energy calculations using a plane-wave basis set. *Phys. Rev. B* **54**, 11169–11186 (1996).
73. Blöchl, P. E. Projector augmented-wave method. *Phys. Rev. B* **50**, 17953–17979 (1994).
74. Perdew, J. P. et al. Restoring the density-gradient expansion for exchange in solids and surfaces. *Phys. Rev. Lett.* **100**, 136406 (2008).
75. Perdew, J. P., Burke, K. & Wang, Y. Generalized gradient approximation for the exchange-correlation hole of a many-electron system. *Phys. Rev. B* **54**, 16533–16539 (1996).
76. Hellman, O. & Abrikosov, I. A. Temperature-dependent effective third-order interatomic force constants from first principles. *Phys. Rev. B* **88**, 144301 (2013).
77. Kim, D. S. et al. Nuclear quantum effect with pure anharmonicity and the anomalous thermal expansion of silicon. *Proc. Natl. Acad. Sci. USA* **115**, 1992–1997 (2018).
78. Shulumba, N., Hellman, O. & Minnich, A. J. Lattice thermal conductivity of polyethylene molecular crystals from first-principles

including nuclear quantum effects. *Phys. Rev. Lett.* **119**, 185901 (2017).
79. Errea, I., Calandra, M. & Mauri, F. Anharmonic free energies and phonon dispersions from the stochastic self-consistent harmonic approximation: application to platinum and palladium hydrides. *Phys. Rev. B* **89**, 064302 (2014).
80. Tadano, T., Gohda, Y. & Tsuneyuki, S. Anharmonic force constants extracted from first-principles molecular dynamics: applications to heat transfer simulations. *J. Phys. Condens. Matter* **26**, 225402 (2014).
81. Tadano, T. & Tsuneyuki, S. Self-consistent phonon calculations of lattice dynamical properties in cubic $SrTiO_3$ with first-principles anharmonic force constants. *Phys. Rev. B* **92**, 054301 (2015).
82. Hellman, O., Abrikosov, I. A. & Simak, S. I. Lattice dynamics of anharmonic solids from first principles. *Phys. Rev. B* **84**, 180301 (2011).
83. Nelson, L. J., Hart, G. L. W., Zhou, F. & Ozoliņš, V. Compressive sensing as a paradigm for building physics models. *Phys. Rev. B* **87**, 035125 (2013).
84. Tadano, T. & Tsuneyuki, S. Quartic anharmonicity of rattlers and its effect on lattice thermal conductivity of clathrates from first principles. *Phys. Rev. Lett.* **120**, 105901 (2018).
85. Feng, T. & Ruan, X. Quantum mechanical prediction of four-phonon scattering rates and reduced thermal conductivity of solids. *Phys. Rev. B* **93**, 045202 (2016).
86. Han, Z., Yang, X., Li, W., Feng, T. & Ruan, X. FourPhonon: an extension module to ShengBTE for computing four-phonon scattering rates and thermal conductivity. *Comp. Phys. Commun.* **270**, 108179 (2022).
87. Tamura, S. -i Isotope scattering of dispersive phonons in Ge. *Phys. Rev. B* **27**, 858–866 (1983).
88. Allen, P. B. & Feldman, J. L. Thermal conductivity of disordered harmonic solids. *Phys. Rev. B* **48**, 12581–12588 (1993).
89. Li, W., Carrete, J., A. Katcho, N. & Mingo, N. ShengBTE: a solver of the Boltzmann transport equation for phonons. *Computer Phys. Commun.* **185**, 1747–1758 (2014).
90. Ganose, A. M. et al. Atomate2: modular workflows for materials science. *Digital Discov.* **4**, 1944–1973 (2025).
91. Shen X., Guilmeau E., Koza M. M., Weber F. Lattice dynamics and Ag diffusion in Ag_3SbS_3. *Institut Laue-Langevin (ILL)* https://doi.org/10.5291/ILL-DATA.7-01-592 (2024).
92. Momma, K. & Izumi, F. VESTA: a three-dimensional visualization system for electronic and structural analysis. *J. Appl. Crystallogr.* **41**, 653–658 (2008).

Acknowledgements

X.S. acknowledges funding supported by National Youth Talent Project (Overseas) and the Fundamental Research Funds for the Central Universities (G2025KY05141), and the European Union's Horizon 2020 research and innovation program under the Marie Sklodowska-Curie grant agreement No 101034329 and the WINNING Normandy Program. X.S. and M.M.K acknowledge the European Neutron Source Institut Laue Langevin (ILL), Grenoble, France for the provision of neutron beamtime of our proposal (No.7-01-592)[91] at beamline Panther. We thank Geoffroy Hautier (Rice University, formerly at Dartmouth College) for thoughtful review of the manuscript and his insightful suggestions. We thank Hrushikesh Sahasrabuddhe (University of California, Berkeley) for his valuable discussions on the machine-learning calculations. We also thank Dr. Mani Jayaraman (Northwestern Polytechnical University) for his assistance with data collection.

Author contributions

X.S. conceived the idea, and X.S. and J.Z. designed the project. Materials synthesis and characterizations: X.S., P.L., J.H., P.B., B.R., J.W., J.L., P.L., C.C., and E.G. Theory and modeling: X.S. and J.Z. Inelastic neutron scattering measurements and analysis: X.S., M.M.K. DFT and high-throughput calculations: J.Z. Manuscript draft: X.S. and J.Z. with input from the other co-authors; Review and editing: X.S., J.Z. and other co-authors.

Competing interests

The authors declare no competing interests.

Additional information

Supplementary information The online version contains supplementary material available at https://doi.org/10.1038/s41467-025-67333-z.

Correspondence and requests for materials should be addressed to Xingchen Shen or Emmanuel Guilmeau.

Peer review information *Nature Communications* thanks the anonymous reviewer(s) for their contribution to the peer review of this work. A peer review file is available.